# A Comparative Analysis of MU-NOMA IRS-and Relay-Assisted Symbiotic Radio IoT Networks

Derek Kwaku Pobi Asiedu, Samuel Kwamena, Prince Anokye, Mustapha Benjillali, Kyoung-Jae Lee, Samir Saoudi

# A Comparative Analysis of MU-NOMA IRS- and Relay-Assisted Symbiotic Radio IoT Networks

Derek Kwaku Pobi Asiedu*, Samuel Kwamena. Menanor†, Prince Anokye†, Mustapha Benjillali*‡, Kyoung-Jae Lee†, and Samir Saoudi*

*Lab-STICC, IMT-Atlantique, 29238 Brest, France. Emails: kwakupobi@ieee.org, and samir.saoudi@imt-atlantique.fr

†Department of Electronic Engineering, Hanbat National University, 34158 Daejeon, South Korea. Emails: smenanor@htu.edu.gh, princemcanokye@yahoo.com, and kyoungjae@hanbat.ac.kr

‡Department of Communication Systems, INPT, 10100 Rabat, Morocco. Email: benjillali@ieee.org

***Abstract*—This work analyzes the energy-efficiency (EE) performance of two types of energy harvesting secondary networks (SN) in a symbiotic radio network (SRN) relationship with a multi-user non-orthogonal multi-access primary network. The first SN type comprises of a multiple secondary transmitters semi-passive (i.e., equipped with sensing capabilities) intelligent reflective surface using backscatter technology to communicate with a secondary receiver. While the second SN type consists of multiple multi-antenna decode-and-forward relaying sensors communicating with an SRN. Closed-form expressions are derived for the achievable EE, which correlate exactly with Monte Carlo simulations. In addition, the IRS-enabled SRN shows higher EE compared to the relay-enabled SRN due to lower power consumption and higher reflective surface spatial diversity.**

***Index Terms*—Energy-efficiency, symbiotic radio, energy harvesting, intelligent reflecting surface, decode-and-forward relay.**

## I. Introduction

The global data traffic is estimated to grow exponentially in the coming years with a substantial increase in device density within the Internet-of-Things (IoT) infrastructure. According to research, a significant amount of dedicated spectrum is required to support emerging wireless services in IoT networks (IoTNs) [1]. However, existing wireless communication services have exhausted and strained the scarce radio spectrum. Hence, resulting in a spectrum resource scarcity problem. Therefore, innovative technologies promoting sustainable IoTNs in terms of efficient wireless communication resources (spectrum and energy) usage are highly encouraged in next-generation wireless communication research and development.

To promote efficient use and management of IoTN spectrum, two promising spectrum sharing technologies being studied are cognitive (CRNs) and symbiotic radio networks (SRNs). Basically, both technologies consider two or more sub-network co-existing (e.g., primary (PN), secondary (SN) and tertiary (TN) networks) and sharing the same resources such as spectrum, time and power [2]. However, a major issue with this technology is the presence and mitigation of inter-node and inter-network interference [2], [3], which is reduced in their non-resource sharing counterpart. To go beyond spectrum management, SRN has been combined with other technologies such as backscatter (BC) (efficient energy usage) communication, multi-user multi-access techniques such as non-orthogonal multiple access techniques (NOMA) (efficient spectrum usage), and assistive technologies (spatial diversity, coverage improvement and throughput improvement) such as user-relaying or intelligent reflective surfaces (IRS) for better quality-of-service (QoS) such as spatial diversity, improve reliability and throughput, and reduce latency [4]. Several works combining SRN, BC, NOMA and IRS-assisted have focused on outage probability [5], [6], and QoS (rate [3] spectrum-efficiency (SE) and energy-efficiency (EE) [7]) optimization.

Focusing more on improving energy efficiency through radio frequency energy harvesting (EH), the concurrent wireless information and power transfer (WPCN) and the simultaneous wireless information and power transfer (SWIPT) for EH by IoTN communication nodes has been proposed and undergoing intensive research for its applicability [8]–[10]. SWIPT with its sub-technologies of time switching ratio (TSR) and power splitting ratio (PSR) have been considered in SRN combined with NOMA, IRS-assisted or BC technologies [7], [11]. Authors in [7] formulated an optimization problem to maximize the EE in a secure IRS-aided SWIPT network by jointly optimizing the transmit beamforming vectors and the artificial noise (AN) covariance matrix at the access point, and the IRS phase shifts. An adopted hybrid TSR+PSR SWIPT non-linear EH model with particle swarm optimization technique implemented to maximize EE was considered in [11].

Motivated by the discussions above, this work integrates (i) an PN of NOMA multi-antenna primary transmitter (PT) communicating with multiple single antenna primary receivers (PRs) and an SN consisting of multiple secondary transmitters (STs) communicating with a single antenna secondary receiver (SR) in an EE SRN. Unlike the works in [3], [5]–[7], this work considers EH at the STs and extend the simple rectifier EH model in [12] to a multi-stage rectifier EH model to mimic practical EH circuit design. In addition, this work considers two scenarios based on the STs type, namely, (i) scenario 1: the STs are multi-antenna PSR SWIPT decode-and-forward (DF) relay sensor devices, and (ii) scenario 2: the STs are EH semi-passive IRS devices (equipped with a sensor) transmitting their data and reflecting the PT data using BC technology. Hence, the combination of the multiple EH IRS, the SWIPT relaying SRN and the multi-stage EH model in SRNs is new and have

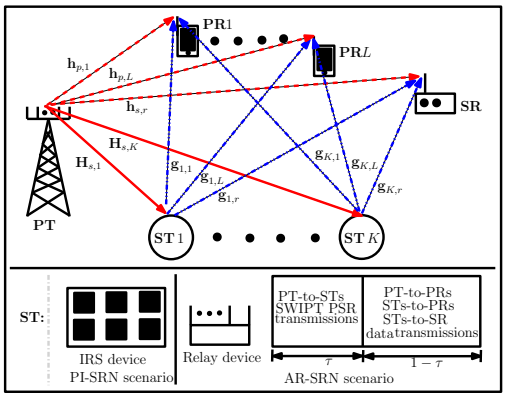


Fig. 1. Considered SRN system model

not been studied separately or combined in existing works such as [3], [5]–[7], [11]. In addition to the two proposed SRN system models, the EE analytical derivation for both scenarios are presented and shown to agree with Monte Carlo simulation.

*Notations*: Bold face lower case and upper case letters represent vectors and matrices, respectively. $\mathbb{E}.$, $\text{tr}(.)$ and $(.)^H$ denote the expectation, trace and Hermitian operators, respectively. $a \sim \mathcal{CN}(0, A)$ indicates a circularly symmetric complex Gaussian random variable with mean 0 and covariance $A$.

## II. System Model and Signal Transmission

The two type SN-based SRN models are shown in Fig. 1, where an PN comprises of $N_p$ multi-antenna PT using NOMA technique transmits information through either (i) $K$ multiple EH semi-passive IRS equipped with sensor devices (SDs) (PI-SRN: ST $k$, $k = 1, \ldots, K$) or (ii) multiple antenna EH relay SDs (AR-SRN (STs)) to $L$ multiple single antenna users (PR $l$, $l = 1, \ldots, L$) are studied. The STs consist of the two sensor-enabled assistive devices, that is, either using BC by IRS or DF by relays. The EH STs aim to transmit data to a single antenna SR. In both models, the channel from the PT to PR $l$, ST $k$ and SR are respectively denoted as $\mathbf{h}_{p,l}$, $\mathbf{H}_{s,k}$ and $\mathbf{h}_{s,r}$. The channels from ST $k$ to PR $l$ and SR are defined as $\mathbf{g}_{k,l}$ and $\mathbf{g}_{k,r}$, respectively. The transmitted signals from PT to PR $l$ and ST $k$ to SR are represented as $x_{p,l}$ and $x_{k,r}$, respectively. The detailed signal flow for the two scenarios are as follows.

### A. Passive IRS-Assisted (PI-) SRN Scenario

The PI-SRN system model shown in Fig. 1 consists of $N_p$ antennas PT, $L$ single antenna PRs, $K$ multiple sensing-enabled semi-passive IRS BC devices with $N_k$ reflective elements each and a single antenna SR. The PT transmitted data is defined as $\mathbf{x}_p = \sum_{l=1}^{L} \mathbf{w}_{p,l} x_{p,l}$, where $\mathbf{w}_{p,l} \in \mathbb{C}^{N_p \times 1}$ is the PT to PR $l$ beamforming vector. Denoting $\{(z_1, z_2)\} \in \{(p, l), (s, r)\}$, after PT and STs BC simultaneous transmission, the received signals at PR $l$ and SR are expressed as

$$y_{z_1,z_2} = \left(\mathbf{h}_{z_1,z_2}^H + \sum_{k=1}^{K} \mathbf{g}_{k,z_2}^H \boldsymbol{\Theta}_k^{1/2} \mathbf{H}_{s,k} x_{k,r}\right) \sum_{l=1}^{L} \mathbf{w}_{p,l} x_{p,l} + n_{z_2}. \quad (1)$$

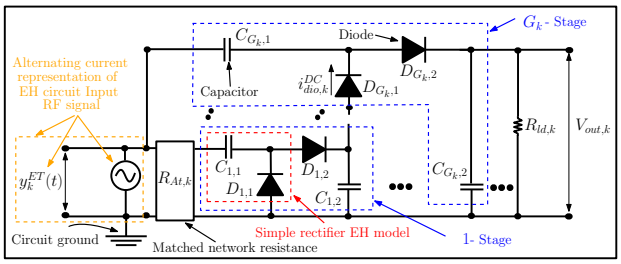


Fig. 2. EH circuit schematic diagram

The antenna noise is $n_{z_2} \sim \mathcal{CN}(0, \sigma_{z_2}^2)$. The IRSs harvest power (circuit power ($P_{\text{cir},k}$) used for IRS signal modulation) from the refracted PT RF signal, which is given as

$$P_{\text{cir},k} \approx \frac{G_k^2 R_{At,k}^2 \sum_{l=1}^{L} \hat{v}_{k,l}}{4 R_{ld,k} \alpha_k^2 V_{T,k}^2} + \frac{G_k^2 R_{At,k}^3 \sum_{l=1}^{L} \bar{v}_{k,l}}{32 R_{ld,k} \alpha_k^4 V_{T,k}^4} + \frac{G_k^2 R_{At,k}^4 \sum_{l=1}^{L} \tilde{v}_{k,l}}{1024 R_{ld,k} \alpha_k^6 V_{T,k}^6}, \quad (2)$$

where, $\hat{v}_{k,l} = |(\mathbf{i} - \boldsymbol{\theta}_k)^{\frac{1}{2}H} \mathbf{H}_{s,k} \mathbf{w}_{p,l}|^4$, $\bar{v}_{k,l} = \hat{v}_{k,l}^{\frac{3}{2}}$, $\tilde{v}_{k,l} = \hat{v}_{k,l}^2$. $\boldsymbol{\theta}_k$ and $\mathbf{i}$ are vectors containing the reflection coefficients of ST $k$ and ones of length $N_k$, respectively. Here, $G_k = 4$, $R_{At,k} = 50\Omega$, $R_{ld,k} = 10^5\Omega$, $V_{T,k} = 25.86$mV, and $\alpha_k = 1.05$ are the number of multi-stages, antenna matched resistance, the load resistance, the diode thermal voltage, and the ideality factor of the EH circuit. (2) is acquired by extending the simple rectifier [12] to the multi-stage rectifier EH model depicted in Fig. 2.

Assuming perfect channel state information at the PTs, PRs and SR, and using perfect linear detection and successive interference cancellation (SIC) [1] for decoding the PT and STs signals at PR $l$ and the SR, the achieved signal-to-interference-noise-ratio (SINR) at the PR $l$ and the SR for the ST $k$ sensor data are deduced respectively as [1]

$$\gamma_l = \frac{A_l}{B_l + C_l + \sigma_l^2} \text{ and } \gamma_{k,r} = \frac{A_{k,r}}{B_{k,r} + C_{k,r} + \sigma_r^2}, \quad (3)$$

where $A_l = |\mathbf{h}_{p,l}^H \mathbf{w}_{p,l}|^2 + \sum_{k=1}^{K} |\mathbf{g}_{k,l}^H \boldsymbol{\Theta}_k^{1/2} \mathbf{H}_{s,k} \mathbf{w}_{p,l}|^2$, $B_l = \sum_{j \neq l}^{L} \alpha_{l,j} (|\mathbf{h}_{p,l}^H \mathbf{w}_{p,j}|^2 + \sum_{k=1}^{K} |\mathbf{g}_{k,l}^H \boldsymbol{\Theta}_k^{1/2} \mathbf{H}_{s,k} \mathbf{w}_{p,j}|^2)$, $B_{k,r} = \sum_{l=1}^{L} (|\mathbf{h}_{s,r}^H \mathbf{w}_{p,l}|^2 + \sum_{k=1}^{K} \beta_{k,l,j} |\mathbf{g}_{j,r}^H \boldsymbol{\Theta}_j^{1/2} \mathbf{H}_{s,j} \mathbf{w}_{p,l}|^2)$, $C_l = \sum_{j=1}^{L} \sum_{k=1}^{K} \alpha_{l,j,k} |\mathbf{g}_{k,l}^H \boldsymbol{\Theta}_k^{1/2} \mathbf{H}_{s,k} \mathbf{w}_{p,j}|^2$, $C_{k,r} = \sum_{j \neq k}^{K} \sum_{l=1}^{L} \beta_{k,j} |\mathbf{g}_{j,r}^H \boldsymbol{\Theta}_j^{1/2} \mathbf{H}_{s,j} \mathbf{w}_{p,l}|^2$, and $A_{k,r} = \sum_{l=1}^{L} |\mathbf{g}_{k,r}^H \boldsymbol{\Theta}_k^{1/2} \mathbf{H}_{s,k} \mathbf{w}_{p,l}|^2$. $\{\alpha_{l,j}, \alpha_{l,j,k}\} \in [0, 1]$ are the SIC successful decoding factors for PR $j$ and ST $k$ during SIC information decoding at PR $l$. $\{\beta_{k,j}, \beta_{k,l,j}\} \in [0, 1]$ are the SIC factors for PR $j$ and ST $i$ during SIC information decoding at SR for ST $k$ received signal. $A_l$ is PR $l$ desired decoded signal, while $B_l$ and $C_l$ are respectively the set of PRs ($\{\text{PR}_j\}_{j \neq l}^{L}$) and STs ($\{\text{ST}_k\}_{k=1}^{K}$) interference signals at PR $l$ during data decoding. $A_{k,r}$ is the desired signal of ST $k$ at SR, while $B_{k,r}$ and $C_{k,r}$ are respectively the set of PRs ($\{\text{PR}_l\}_{l=1}^{L}$) and STs ($\{\text{ST}_j\}_{j \neq k}^{l}$) interference signals present at SR during ST $k$ data decoding. The rates based on (3) are

defined as $R_l = \log_2(1+\gamma_l)$ and $R_{k,r} = \log_2(1+\gamma_{k,r})$. The system achieved EE is deduced as

$$\text{EE}_{\text{PI}} = \frac{\sum_{l=1}^{L} R_l + \sum_{k=1}^{K} R_{k,r}}{\sum_{l=1}^{L} \|\mathbf{w}_{p,l}\|^2 + \sum_{k=1}^{K} P_{\text{cir},k}}. \tag{4}$$

### *B. Active Relay-Assisted (AR-) SRN Scenario*

For the AR-SRN system as shown in Fig 1, STs are replaced with $K$ PSR SWIPT EH SDs with $N_k$ antenna, which relay the PT signals to the PRs using DF relaying and the Time Division Duplex (two time slots). Here, the relaying STs use the PSR $\rho_k$ SWIPT scheme to harvest energy and decode the PT transmitted RF signals in the first time slot ($\tau$). In the second phase ($1-\tau$), the STs combine their own signals with the decoded PT signals, and transmit them to the PRs and SR. At the same time (phase 2), the PT transmits data to the PRs.

In time slot $\tau$, the PT data ($\mathbf{X}_p = \sum_{l=1}^{L}\sum_{k=1}^{K} \mathbf{W}_{s,k} x_{p,l}$) received signal at ST $k$ is written as $\mathbf{Y}_k = \mathbf{H}_{s,k}^H \mathbf{X}_p + \mathbf{N}_k$, where $\mathbf{W}_{s,k} \in \mathbb{C}^{N_p \times N_k}$ represents the beamforming matrix from PT to ST $k$. At ST $k$, the PT received RF signal is split using the PSR $\boldsymbol{\rho}_k$ vector into two, a portion for ID and forwarding ($\sqrt{\boldsymbol{\rho}_k}^H \mathbf{Y}_k \bar{\mathbf{W}}_k$), and the other portion for EH ($\sqrt{(\mathbf{i}-\boldsymbol{\rho}_k)}^H \mathbf{Y}_k$), where $\bar{\mathbf{W}}_k$ is ST $k$ receive filter. This implies that, ST $k$ harvested energy, $v_k$, is deduced as [12]

$$\begin{aligned} v_k \approx{}& \frac{\tau G_k^2 R_{At,k}^2 \sum_{k=1}^{K} \hat{v}_k}{4(1-\tau) R_{ld,k} \alpha_k^2 V_{T,k}^2} + \frac{\tau G_k^2 R_{At,k}^3 \sum_{k=1}^{K} \bar{v}_k}{32(1-\tau) R_{ld,k} \alpha_k^4 V_{T,k}^4} \\ &+ \frac{\tau G_k^2 R_{At,k}^4 \sum_{k=1}^{K} \tilde{v}_k}{1024(1-\tau) R_{ld,k} \alpha_k^6 V_{T,k}^6}, \end{aligned} \tag{5}$$

where, $\hat{v}_k = |(\mathbf{i}-\boldsymbol{\rho}_k)^{\frac{1}{2}H} \mathbf{H}_{s,k} \mathbf{W}_{s,k} \mathbf{W}_{s,k}^H \mathbf{H}_{s,k}^H (\mathbf{i}-\boldsymbol{\rho}_k)^{\frac{1}{2}}|^2$, $\bar{v}_k = \hat{v}_k^{\frac{3}{2}}$, $\tilde{v}_k = \hat{v}_k^2$. The initial PT data $\mathbf{x}_p$ is decoded (DF) from the ID portion received at ST $k$, and this decoded signal is re-transmitted using $v_k$ in the time slot $(1-\tau)$.

During $(1-\tau)$, ST $k$ forwards the decoded PT signal and its own signal ($\mathbf{x}_{s,k} = \mathbf{w}_{k,r} x_{k,r} + \sum_{l=1}^{L} \mathbf{w}_{k,l} x_{p,l}$) to the PRs and the SR, using the beamformers $\mathbf{w}_{k,l} \in \mathbb{C}^{N_k \times 1}$ and $\mathbf{w}_{k,r} \in \mathbb{C}^{N_k \times 1}$. Simultaneously, the PT re-transmits data $\mathbf{x}_p$ to the PRs. Hence, the received signal at PR $l$ and SR is given as

$$\begin{aligned} &\bar{y}_{k,z_1} = \\ &\sum_{k=1}^{K} \mathbf{g}_{k,z_1}^H \Big( \mathbf{w}_{k,r} x_{k,r} + \sum_{l=1}^{L} \mathbf{w}_{k,l} x_{p,l} \Big) + \sum_{l=1}^{L} \mathbf{h}_{z_2} \mathbf{x}_p + \bar{n}_{z_1}, \end{aligned} \tag{6}$$

where $v_k \geq \sum_{l=1}^{L} \|\mathbf{w}_{k,l}\|^2 + \|\mathbf{w}_{k,r}\|^2$, $z_2 \in \{(p,l),(s,r)\}$ and $z_1 \in \{l,r\}$. Using SIC, the SINR for PR $l$ and ST $k$ data decoding are respectively[1]

$$\gamma_l = \frac{N_l}{A_l + B_l + \sigma_l^2} \text{ and } \gamma_{k,r} = \frac{N_{k,r}}{A_{k,r} + B_{k,r} + \sigma_r^2}, \tag{7}$$

[1]In DF relaying, $R_l = \log_2(1 + \min\{\hat{\gamma}_l, \gamma_l\})$, where $\gamma_l$ in (7), $\hat{\gamma}_l = \sqrt{\boldsymbol{\rho}_k}^H \mathbf{H}_{s,k} \mathbf{W}_{s,k} \bar{\mathbf{W}}_k \mathbf{R}^{-1} \bar{\mathbf{W}}_k^H \mathbf{W}_{s,k}^H \mathbf{H}_{s,k}^H \sqrt{\boldsymbol{\rho}_k}$ acquired in time slot $\tau$ and $\mathbf{R} = (\sum_{j\neq k}^{K} \sqrt{\boldsymbol{\rho}_k}^H \mathbf{H}_{s,k} \mathbf{W}_{s,j} \bar{\mathbf{W}}_k \bar{\mathbf{W}}_k^H \mathbf{W}_{s,j}^H \mathbf{H}_{s,k}^H \sqrt{\boldsymbol{\rho}_k} + \mathbf{I}\sigma_k^2)$. By observation, $\hat{\gamma}_l > \gamma_l$ because of $\tau$ and $(1-\tau)$ transmit power relation $P_p >> v_k$ and larger interference during $(1-\tau)$, hence $R_l = \log_2(1+\gamma_l)$.

with variables $N_{k,r} = |\mathbf{g}_{k,r}^H \mathbf{w}_{k,r}|^2$, $N_l = |\mathbf{h}_{p,l}^H \mathbf{w}_{p,l}|^2 + \sum_{k=1}^{K} |\mathbf{g}_{k,l}^H \mathbf{w}_{k,l}|^2$, $B_l = \sum_{k=1}^{K}\sum_{j=1}^{L} \alpha_{l,k} |\mathbf{g}_{k,l}^H \mathbf{w}_{k,j}|^2$, $A_{k,r} = \sum_{j\neq k}^{K} \hat{\beta}_{k,j} |\mathbf{g}_{k,r}^H \mathbf{w}_{j,r}|^2$, $A_l = \sum_{k=1}^{K}\sum_{j\neq l}^{L} \bar{\alpha}_{l,j,k} |\mathbf{g}_{k,l}^H \mathbf{w}_{k,j}|^2 + \sum_{j\neq l}^{L} \bar{\alpha}_{l,j} |\mathbf{h}_{p,l}^H \mathbf{w}_{p,j}|^2$, $B_{k,r} = \sum_{i=1}^{K}\sum_{j=1}^{L} \bar{\beta}_{k,i,j} |\mathbf{g}_{i,r}^H \mathbf{w}_{i,j}|^2 + \sum_{j=1}^{L} \bar{\beta}_{k,j} |\mathbf{h}_{s,r}^H \mathbf{w}_{p,j}|^2$. Here $\{\bar{\alpha}_{l,j,k}, \alpha_{l,k}\} \in [0,1]$ are the SIC factors for PR $j$ and ST $k$ during SIC information decoding at PR $l$. $\{\hat{\beta}_{k,j}, \bar{\beta}_{k,i,j}\} \in [0,1]$ are the SIC factors for PR $j$ and ST $i$ during SIC information decoding at the SR for ST $k$ received signal. Also, $A_l$ and $B_l$ are interference noises power at PR $l$ induced by the received signals of other PRs and the STs, respectively. $A_{k,r}$ and $B_{k,r}$ are the interference noises power at SR induced by the received signals of PRs and other STs when decoding ST $k$ received signals, respectively.

From (7) achievable rates are respectively deduced as $R_l = (1-\tau)\log_2(1+\gamma_l)$ and $R_{k,r} = (1-\tau)\log_2(1+\gamma_{k,r})$ [13]. The system achieved EE is deduced as

$$\text{EE}_{\text{AR}} = \frac{\sum_{l=1}^{L} R_l + \sum_{k=1}^{K} R_{k,r}}{\sum_{k=1}^{K} \text{tr}(\mathbf{W}_{s,k} \mathbf{W}_{s,k}^H) + \sum_{l=1}^{L} \|\mathbf{w}_{p,l}\|^2 + \sum_{k=1}^{K} v_k}. \tag{8}$$

(8) denominator, from left to right are the PT-STs, PT-PRs and STs-{PRs+SR} transmission powers consumed, respectively.

## III. Analytical Derivation

The PI- and AR-SRN beamformers, harvested energy and average SINR analysis are presented here to study the PI- and AR-SRN attributes. The channels are modeled as Rician fading with their expectations defined as [3], [14]–[16];

$$\mathbb{E}[\mathbf{h}_{z_1}] \approx \left( \frac{A_{z_1} \left( \frac{d_{z_1}}{d_0} \right)^{-\zeta_{z_1}}}{(\mu_{z_1}+1)} \right)^{1/2} (\mu_{z_1}^{1/2} + \chi_{z_1}) N_p, \tag{9}$$

$$\mathbb{E}[\mathbf{g}_{z_2}] \approx \left( \frac{A_{z_2} \left( \frac{d_{z_2}}{d_0} \right)^{-\zeta_{z_2}}}{(\mu_{z_2}+1)} \right)^{1/2} (\mu_{z_2}^{1/2} + \chi_{z_2}) N_k, \tag{10}$$

$$\mathbb{E}[\mathbf{H}_{z_3}] \approx \left( \frac{A_{z_3} \left( \frac{d_{z_3}}{d_0} \right)^{-\zeta_{z_3}}}{(\mu_{z_3}+1)} \right)^{1/2} (\mu_{z_3}^{1/2} + \chi_{z_3}) N_p N_k, \tag{11}$$

where $\mu_z$ represents the Rician factor, $z \in \{z_1, z_2, z_3\}$, $z_1 \in \{(p,l),(s,r)\}$, $z_2 \in \{(k,l),(k,r)\}$, $z_3 \in \{(s,k)\}$ and $(\chi_{z_1}, \chi_{z_2}, \chi_{z_3}) \sim \mathcal{CN}(0,1)$ are the small-scale fading components modelled as Gaussian variables [15], [16]. Each PSR ($\rho$) and reflection co-efficient ($\theta$) are constant. The transmitters use equal power allocation with maximum ratio transmission for data transmission, that is, $\mathbf{w}_{p,l} = \frac{P_p \mathbf{h}_{p,l}}{L\|\mathbf{h}_{p,l}\|}$, $\mathbf{W}_{z_3} = \frac{P_p \mathbf{H}_{z_3}}{K\|\mathbf{H}_{z_3}\|}$, and $\mathbf{w}_{z_2} = \frac{v_k \mathbf{g}_{z_2}}{(L+1)\|\mathbf{g}_{z_2}\|}$, implying, $\mathbb{E}[\mathbf{w}_{p,l}] = \frac{P_p}{L}\mathbb{E}\left[\frac{\mathbf{h}_{p,l}}{\|\mathbf{h}_{p,l}\|}\right]$, $\mathbb{E}[\mathbf{W}_{z_3}] = \frac{P_p}{K}\mathbb{E}\left[\frac{\mathbf{H}_{z_3}}{\|\mathbf{H}_{z_3}\|}\right]$, and $\mathbb{E}[\mathbf{w}_{z_2}] = \frac{v_k}{L+1}\mathbb{E}\left[\frac{\mathbf{g}_{z_2}}{\|\mathbf{g}_{z_2}\|}\right]$.

### *A. PI-SRN Scenario*

For the PN, the SINR expectation is defined as

$$\mathbb{E}[\gamma_l] \approx \mathbb{E}[A_l]/(\mathbb{E}[B_l] + \mathbb{E}[C_l] + 1), \tag{12}$$

with

$$\mathbb{E}[A_l] \approx \frac{P_p}{L}\frac{\left(A_{p,l}\left(\frac{d_{p,l}}{d_0}\right)^{-\zeta_{p,l}}\right)}{(\mu_{p,l}+1)}(\mu_{p,l}^{1/2}+\chi_{p,l})^2 N_p^2 + \sum_{k=1}^{K}\frac{\theta N_k P_p}{L}\frac{\left(A_{k,l}A_{s,k}\left(\frac{d_{k,l}}{d_0}\right)^{-\zeta_{k,l}}\left(\frac{d_{s,k}}{d_0}\right)^{-\zeta_{s,k}}\right)}{(\mu_{k,l}+1)(\mu_{s,k}+1)} \times (\mu_{k,l}^{1/2}+\chi_{k,l})^2(\mu_{s,k}^{1/2}+\chi_{s,k})^2 N_p^2 N_k^2, \quad (13)$$

$$\mathbb{E}[B_l] \approx \frac{(L-1)P_p}{L}\frac{\left(A_{p,l}\left(\frac{d_{p,l}}{d_0}\right)^{-\zeta_{p,l}}\right)}{(\mu_{p,l}+1)}(\mu_{p,l}^{1/2}+\chi_{p,l})^2 N_p^2 + \sum_{k=1}^{K}\frac{P_p(L-1)}{L}\frac{\left(A_{k,l}A_{s,k}\left(\frac{d_{k,l}}{d_0}\right)^{-\zeta_{k,l}}\left(\frac{d_{s,k}}{d_0}\right)^{-\zeta_{s,k}}\right)}{(\mu_{k,l}+1)(\mu_{s,k}+1)} \times \theta N_k(\mu_{k,l}^{1/2}+\chi_{k,l})^2(\mu_{s,k}^{1/2}+\chi_{s,k})^2 N_p^2 N_k^2, \text{ and} \quad (14)$$

$$\mathbb{E}[C_l] \approx \sum_{k=1}^{K}\frac{\left(A_{k,l}A_{s,k}\left(\frac{d_{k,l}}{d_0}\right)^{-\zeta_{k,l}}\left(\frac{d_{s,k}}{d_0}\right)^{-\zeta_{s,k}}\right)}{(\mu_{k,l}+1)(\mu_{s,k}+1)} \times \theta N_k P_p(\mu_{k,l}^{1/2}+\chi_{k,l})^2(\mu_{s,k}^{1/2}+\chi_{s,k})^2 N_p^2 N_k^2. \quad (15)$$

Now, for the SN, the SINR expectation is given as

$$\mathbb{E}[\gamma_{k,r}] \approx \mathbb{E}[A_{k,r}]/(\mathbb{E}[B_{k,r}]+\mathbb{E}[C_{k,r}]+1), \text{ where} \quad (16)$$

$$\mathbb{E}[A_{k,r}] \approx \theta N_k P_p \frac{\left(A_{k,r}A_{s,k}\left(\frac{d_{k,r}}{d_0}\right)^{-\zeta_{k,r}}\left(\frac{d_{s,k}}{d_0}\right)^{-\zeta_{s,k}}\right)}{(\mu_{k,r}+1)(\mu_{s,k}+1)} \times (\mu_{k,r}^{1/2}+\chi_{k,r})^2(\mu_{s,k}^{1/2}+\chi_{s,k})^2 N_p^2 N_k^2, \quad (17)$$

$$\mathbb{E}[B_{k,r}] \approx P_p\frac{\left(A_{s,r}\left(\frac{d_{s,r}}{d_0}\right)^{-\zeta_{s,r}}\right)}{(\mu_{s,r}+1)}(\mu_{s,r}^{1/2}+\chi_{s,r})^2 N_p^2 + \sum_{j=1}^{K}\theta N_j P_p\frac{\left(A_{j,r}A_{s,j}\left(\frac{d_{j,r}}{d_0}\right)^{-\zeta_{j,r}}\left(\frac{d_{s,j}}{d_0}\right)^{-\zeta_{s,j}}\right)}{(\mu_{j,r}+1)(\mu_{s,j}+1)} \times (\mu_{j,r}^{1/2}+\chi_{j,r})^2(\mu_{s,j}^{1/2}+\chi_{s,j})^2 N_p^2 N_j^2, \text{ and} \quad (18)$$

$$\mathbb{E}[C_{k,r}] \approx \sum_{j\neq k}^{K}\frac{\left(A_{j,r}A_{s,j}\left(\frac{d_{j,r}}{d_0}\right)^{-\zeta_{j,r}}\left(\frac{d_{s,j}}{d_0}\right)^{-\zeta_{s,j}}\right)}{(\mu_{j,r}+1)(\mu_{s,j}+1)} \times \theta N_j P_p(\mu_{j,r}^{1/2}+\chi_{j,r})^2(\mu_{s,j}^{1/2}+\chi_{s,j})^2 N_p^2 N_j^2. \quad (19)$$

For the energy harvesting power available at the IRS, we have

$$\mathbb{E}[\hat{v}_{k,l}] \approx P_p(1-\theta)^2 N_k^2(\mu_{s,k}^{1/2}+\chi_{s,k})^4 N_p^4 N_k^4 \times \left(A_{s,k}\left(\frac{d_{s,k}}{d_0}\right)^{-\zeta_{s,k}}\right)^2/(\mu_{s,k}+1)^2, \quad (20)$$

### *B. AR-SRN Scenario*

The second time slot PR average SINR is expressed as

$$\mathbb{E}[\bar{\gamma}_l] \approx \mathbb{E}[N_l]/(\mathbb{E}[A_l]+\mathbb{E}[B_l]+1), \text{ with} \quad (21)$$

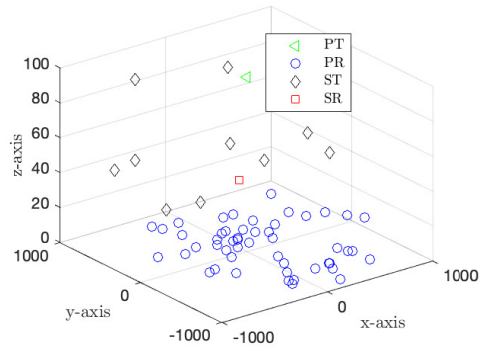


Fig. 3. A simulation of the SRN topology

$$\mathbb{E}[B_l] \approx \sum_{k=1}^{K}\frac{v_k N_k^2}{L+1}\frac{\left(A_{k,l}\left(\frac{d_{k,l}}{d_0}\right)^{-\zeta_{k,l}}\right)}{(\mu_{k,l}+1)}(\mu_{k,l}^{1/2}+\chi_{k,l})^2. \quad (22)$$

$$\mathbb{E}[N_l] \approx \sum_{k=1}^{K}\frac{v_k N_k^2}{L+1}\frac{\left(A_{k,l}\left(\frac{d_{k,l}}{d_0}\right)^{-\zeta_{k,l}}\right)}{(\mu_{k,l}+1)}(\mu_{k,l}^{1/2}+\chi_{k,l})^2 + \frac{P_p}{L}\frac{\left(A_{p,l}\left(\frac{d_{p,l}}{d_0}\right)^{-\zeta_{p,l}}\right)}{(\mu_{p,l}+1)}(\mu_{p,l}^{1/2}+\chi_{p,l})^2 N_p^2, \quad (23)$$

$$\mathbb{E}[A_l] \approx \sum_{k=1}^{K}\frac{v_k(L-1)}{L+1}\frac{\left(A_{k,l}\left(\frac{d_{k,l}}{d_0}\right)^{-\zeta_{k,l}}\right)}{(\mu_{k,l}+1)}(\mu_{k,l}^{1/2}+\chi_{k,l})^2 N_k^2 + \frac{P_p(L-1)}{L}\frac{\left(A_{p,l}\left(\frac{d_{p,l}}{d_0}\right)^{-\zeta_{p,l}}\right)}{(\mu_{p,l}+1)}(\mu_{p,l}^{1/2}+\chi_{p,l})^2 N_p^2, \text{ and} \quad (24)$$

Now, the average ST decoded data at SR is deduced as

$$\mathbb{E}[\gamma_{k,R}] \approx \mathbb{E}[N_{k,r}]/(\mathbb{E}[A_{k,r}]+\mathbb{E}[B_{k,r}]+1), \text{ where} \quad (25)$$

$$\mathbb{E}[N_{k,r}] \approx \frac{v_k N_k^2}{L+1}\frac{\left(A_{k,r}\left(\frac{d_{k,r}}{d_0}\right)^{-\zeta_{k,r}}\right)}{(\mu_{k,r}+1)}(\mu_{k,r}^{1/2}+\chi_{k,r})^2, \quad (26)$$

$$\mathbb{E}[A_{k,r}] \approx \sum_{j\neq k}^{K}\frac{v_k N_j^2}{L+1}\frac{\left(A_{j,r}\left(\frac{d_{j,r}}{d_0}\right)^{-\zeta_{j,r}}\right)}{(\mu_{j,r}+1)}(\mu_{j,r}^{1/2}+\chi_{j,r})^2, \quad (27)$$

$$\mathbb{E}[B_{k,r}] \approx \sum_{k=1}^{K}\frac{v_k L N_k^2}{L+1}\frac{\left(A_{k,r}\left(\frac{d_{k,r}}{d_0}\right)^{-\zeta_{k,r}}\right)}{(\mu_{k,r}+1)}(\mu_{k,r}^{1/2}+\chi_{k,r})^2 + P_p\frac{\left(A_{s,r}\left(\frac{d_{s,r}}{d_0}\right)^{-\zeta_{s,r}}\right)}{(\mu_{s,r}+1)}(\mu_{s,r}^{1/2}+\chi_{s,r})^2 N_p^2. \text{ and} \quad (28)$$

$$\mathbb{E}[\hat{v}_k] \approx P_p(1-\rho)^2 N_k^6\frac{\left(A_{s,k}\left(\frac{d_{s,k}}{d_0}\right)^{-\zeta_{s,k}}\right)^2}{(\mu_{s,k}+1)^2}(\mu_{s,k}^{1/2}+\chi_{s,k})^4 N_p^4. \quad (29)$$

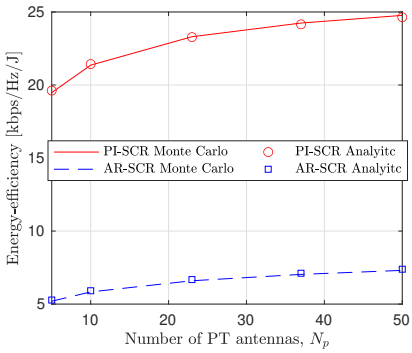


Fig. 4. Average EE vs. $N_p$.

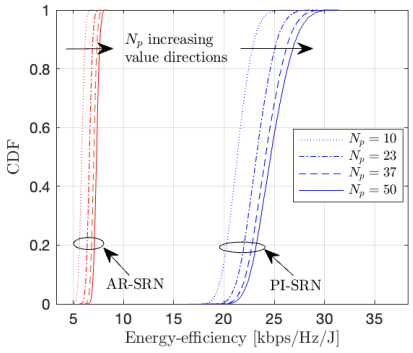


Fig. 5. CDF of EE for varying $N_p$.

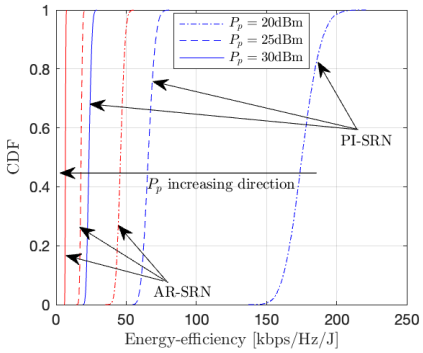


Fig. 6. CDF of EE for varying $P_p$.

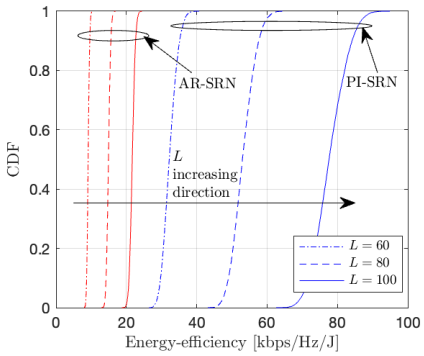


Fig. 7. CDF of EE for varying $L$.

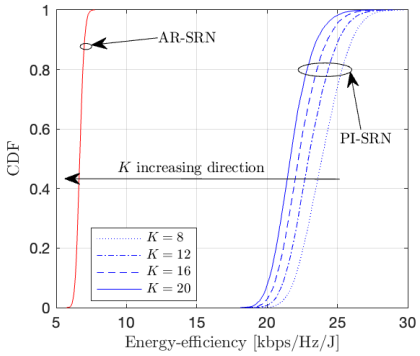


Fig. 8. CDF of EE for varying $K$.

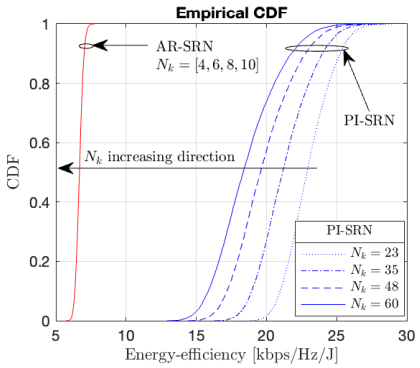


Fig. 9. CDF of EE for varying $N_k$.

## IV. Simulations and Discussions

In this section, simulation results on the EE behavior for both the PI-SRN and AR-SRN with varying system parameters and the Monte Carlo verification are presented. The parameters used for the various simulations are as follows. For the topology consisting of high(wall) mounted sensor network (STs+SR) and BS (PT), and ground level PRs (user devices) with an example shown in Fig. 3, PT is positioned at coordinates $(x_{\text{PT}}, y_{\text{PT}}, z_{\text{PT}}) = (0, 0, 10^2)$m. The SN (STs and SR) and PR devices are randomly distributed within the coordinates $(\{x_{\text{SN}}, y_{\text{SN}}\}, z_{\text{SN}}) \in ([-10^2, 10^2], [10^1, 10^2])$m and $(\{x_{\text{PR}}, y_{\text{PR}}\}, z_{\text{PR}}) \in ([-10^3, 10^3], [10^0, 10^1])$m, respectively. The euclidean distance is used to determine the inter-node distances. For the large-scale model, the geometric attenuation factor is $A_z = 30$dB, $z \in \{(p,l), (s,k), (s,r), (k,l), (k,r)\}$. The Rician factors and pathloss exponents for the SN interactions are $\{\mu_{s,k}, \mu_{k,l}, \mu_{k,r}\} = 3$ and $\{\zeta_{s,k}, \zeta_{k,l}, \zeta_{k,r}\} = 2.5$, and the PN interactions are $\{\mu_{p,l}, \mu_{s,r}\} = 4$ and $\{\zeta_{p,l}, \zeta_{s,r}\} = 3$, respectively. Unless stated, $\{\tau, \rho, \theta\} = 0.5$, $\{$IRS,relay$\}$ : $N_k = \{20, 4\}$, $N_p = 25$, $L = 50$, $K = 10$ and $P_p = 30$dBm. Note, practically deployed SDs currently are not equipped with massive antennas. Hence, for SDs relaying (AR-SRN STs), $N_k \leq 10$ is used. However, a SDs connected to an IRS benefits from the larger reflective elements to improve spatial diversity.

Fig. 4 compares the analytical ((9) to (29)) and Monte Carlo ((4) and (8)) simulation using the average EE against $N_p$ for the PI- and AR-SRN scenarios. From Fig. 4, the analytical and Monte Carlo plots match for both scenarios. It is seen for both cases that the EE increases with increasing $N_p$ . The PI-SRN has a constant gain of 15kbps/Hz/J over the AR-SRN. This is due to the PI-SRN lower power consumption compared to the AR-SRN, as depicted in their EE defined in (4) and (8). Also, the number of IRS reflective elements is larger than the relay antennas, implying higher PI-SRN spatial diversity, leading to better harvested power and achievable rates. The better performance of the PI-SRN over the AR-SRN throughout our discussion is due to the aforementioned factors. Thus, showing the superiority of the PI-SRN over the AR-SRN. The EE CDF for varying $N_p$ is illustrated in Fig. 5 comparing the PI- and AR-SRN. The PI-SRN has higher EE ranging bewteen $[17 - 32]$kbps/Hz/J, while that of the AR-SRN ranges between $[5 - 10]$kbps/Hz/J. Fig. 6 shows the PI- and AR-SRN EE CDF for various $P_p$. It is seen that the EE reduces with increasing $P_p$. From (4) and (8) as the power used (denominator) increases, the rates (numerator) decrease due to increased interference power, leading to a reduction in the EEs. The PI-SRN outperforms the AR-SRN by about 100kbps/Hz/J, 30kbps/Hz/J and 10kbps/Hz/J at 20dBm, 25dBm and 30dBm, respectively. These notable gains emphasize the effectiveness of deploying the semi-passive IRSs in SRN over the AR-SRN.

The PI- and AR-SRN EE CDF for varying $L$ are presented in Fig. 7. As expected, the EE CDF increases with increasing

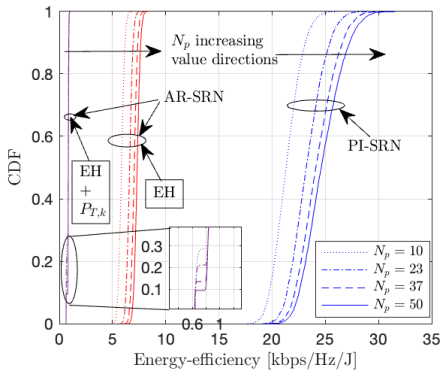


Fig. 10. CDF of EE for varying $N_p$ (Equivalent PI and AR Antenna).

$L$, because the sum-rate ($\sum_{l=1}^{L} R_l$) increases too, at the same amount of $P_p = 30$dBm. Also, the PI-SRN has an EE gain of about 40kbps/Hz/J, 25kbps/Hz/J and 20kbps/Hz/J over the AR-SRN for $L = [60, 80, 100]$, respectively. The EE CDF plot of the PI- and AR-SRN for varying $K$ is presented in Fig. 8. From Fig. 8 as $K$ increases the PI-SRN sees a reduction in EE ($[17 - 28]$kbps/Hz/J), while the EE for AR-SRN remain constant between $[5 - 7]$kbps/Hz/J. The constant AR-SRN EE behavior is due to the PN rates being far larger than the SN rates ((7): $\{\gamma_l, R_l\} >> \{\gamma_{k,r}, R_{k,r}\}$). Also, the EH of each ST is constant as $K$ increases, leading to an increase in the SN interference, which in turn reduces the rate and the EE. The interference behavior also occurs in the PI- and AR-SRN PN, but not as significant because of the higher PI-SRN EH and single transmission time, and the direct link in both PI- and AR-SRN PN. For varying ST (PI-SRN IRS elements and AR-SRN relay antennas), the EE CDF is presented in Fig. 9. The AR-SRN curves are similar because of their small increases in SN rates compared to the far larger AR-SRN PN rates. In contrast, the PI-SRN has significant and comparable PNs and SNs rates. Also, as the PI-SRN $N_k$ increases, the EE reduces because of increased rate interference values.

Fig. 10 shows the CDF vs EE plot where the IRS and relays have equal $N_k$. In addition, the case a relay uses only EH (AR-EH) or EH plus its own transmit power (AR-EHP) are also considered. It is seen that the AR-EH is has similar performance and gap to the PI-SRN as seen in Fig. 4, while the AR-EHP has lesser EE because of the additional transmit power increasing the EE denominator value. Even with equal $N_k$ the AR-SRN achieve marginal gain because of the small energy harvested (transmit power) and high interference. Hence, this study has shown the need to optimize the EH and beamforming, minimizing SN interference, and imposing minimum rate constraints on the SN in AR-SRN to improve performance. The PI- and AR-SRN optimization based on the deductions above is the next step in this research.

## V. Conclusion

The EE performance of EH (i) multiple STs IRS devices backscattering their own and the PN data and (ii) multiple DF relays transmitting their own and the PN data to the PRs and SR were considered. The EE analytical expressions were derived for both cases and these expressions agreed with their Monte Carlo simulations. Also, the PI-SRN outperformed the AR-SRN in terms of EE. An extension of this work involves the EE maximization with resources optimization.

## References


[1] Y.-C. Liang, Q. Zhang, E. G. Larsson, and G. Y. Li, "Symbiotic radio: Cognitive backscattering communications for future wireless networks," *IEEE Trans. Cog. Commun. Network.*, vol. 6, no. 4, pp. 1242–1255, Sep. 2020.

[2] Q. Zhang, Y.-C. Liang, and H. V. Poor, "Reconfigurable intelligent surface assisted MIMO symbiotic radio networks," *IEEE Trans. Commun.*, vol. 69, no. 7, pp. 4832–4846, Mar. 2021.

[3] D. K. P. Asiedu and J.-H. Yun, "Multiuser NOMA with multiple reconfigurable intelligent surfaces for backscatter communication in a symbiotic cognitive radio network," *IEEE Trans. Veh. Technol.*, vol. 72, no. 4, pp. 5300–5316, Dec. 2022.

[4] Q. Wu, S. Zhang, B. Zheng, C. You, and R. Zhang, "Intelligent reflecting surface-aided wireless communications: A tutorial," *IEEE Trans. Commun.*, vol. 69, no. 5, pp. 3313–3351, May 2021.

[5] W. Zhao, G. Wang, S. Atapattu, T. A. Tsiftsis, and C. Tellambura, "Is backscatter link stronger than direct link in reconfigurable intelligent surface-assisted system?" *IEEE Commun. Let.*, vol. 24, no. 6, pp. 1342–1346, Jun. 2020.

[6] C.-B. Le, D.-T. Do, X. Li, Y.-F. Huang, H.-C. Chen, and M. Voznak, "Enabling NOMA in backscatter reconfigurable intelligent surfaces-aided systems," *IEEE Access*, vol. 9, pp. 33 782–33 795, Feb. 2021.

[7] J. Liu, K. Xiong, Y. Lu, D. W. K. Ng, Z. Zhong, and Z. Han, "Energy efficiency in secure IRS-aided SWIPT," *IEEE Wireless Commun. Let.*, vol. 9, no. 11, pp. 1884–1888, Nov. 2020.

[8] B. Talukdar, D. Kumar, and W. Arif, "Performance analysis of a SWIPT enabled cognitive radio sensor network using TS protocol," in *Proc. Advanced Commun. Technol. Sig. Process.*, Dec. 2020, pp. 1–5.

[9] A. A. Nasir, X. Zhou, S. Durrani, and R. A. Kennedy, "Wireless-powered relays in cooperative communications: Time-switching relaying protocols and throughput analysis," *IEEE Trans. Commun.*, vol. 63, no. 5, pp. 1607–1622, Mar. 2015.

[10] X. Zhou, R. Zhang, and C. K. Ho, "Wireless information and power transfer: Architecture design and rate-energy tradeoff," *IEEE Trans. commun.*, vol. 61, no. 11, pp. 4754–4767, Oct. 2013.

[11] A. Prathima, D. S. Gurjar, H. H. Nguyen, and A. Bhardwaj, "Performance analysis and optimization of bidirectional overlay cognitive radio networks with hybrid-SWIPT," *IEEE Trans. Veh. Technol.*, vol. 69, no. 11, pp. 13 467–13 481, Nov. 2020.

[12] S. Shen and B. Clerckx, "Beamforming optimization for MIMO wireless power transfer with nonlinear energy harvesting: RF combining versus DC combining," *IEEE Trans. Wireless Commun.*, vol. 20, no. 1, pp. 199–213, Sep. 2020.

[13] A. K. Shukla, V. Singh, P. K. Upadhyay, A. Kumar, and J. M. Moualeu, "Performance analysis of energy harvesting-assisted overlay cognitive NOMA systems with incremental relaying," *IEEE Open J. Commun. Society*, vol. 2, pp. 1558–1576, Jun. 2021.

[14] D. K. P. Asiedu, H. Lee, and K.-J. Lee, "Simultaneous wireless information and power transfer for decode-and-forward multihop relay systems in energy-constrained IoT networks," *IEEE Internet Things J.*, vol. 6, no. 6, pp. 9413–9426, Dec. 2019.

[15] S. Li, P. J. Smith, P. A. Dmochowski, and J. Yin, "Analysis of analog and digital MRC for distributed and centralized MU-MIMO systems," *IEEE Trans. Veh. Technol.*, vol. 68, no. 2, pp. 1948–1952, Dec. 2018.

[16] H. Tataria, P. J. Smith, M. Matthaiou, and P. A. Dmochowski, "Uplink analysis of large MU-MIMO systems with space-constrained arrays in ricean fading," in *Proc. IEEE Int. Conf. Commun.*, May 2017, pp. 1–7.